GEOCHEMISTRY

Oxidized sediment recycling as a driver for postsubduction porphyry copper formation

Zhiming Yang[1]*, Xiang Sun[2]*, Massimo Chiaradia[3], Yongjun Lu[4,5], Runsheng Yin[6], Zengqian Hou[1], Huawei Li[1], Yiwei Zhou[1]

The mechanisms driving the elevated oxidation state of postsubduction porphyry magmas and porphyry copper mineralization are still not fully understood. We present an integrated study of trace elemental and Mg-Hg isotopic compositions of pre-, syn-, and postcollisional magmatic rocks from the eastern Gangdese belt in southern Tibet. Our findings show increased magmatic oxidation states linked to the enrichment of terrigenous sediments from Neo-Tethys subduction to postcollision, as evidenced by distinctive mass-independent Hg isotope fractionation in postcollisional porphyries (Δ^{199}Hg = −0.25 to 0.22‰) and mantle-derived ultrapotassic rocks (Δ^{199}Hg = −0.54 to 0.25‰) and negative δ^{26}Mg values in ultrapotassic rocks (δ^{26}Mg = −0.51 to −0.04‰). These results suggest that oxidation of postcollisional magmas was driven by the subduction of carbonates and/or sulfates from the Indian plate, enhancing metal enrichment. This finding challenges the traditional view that oceanic subduction primarily drives porphyry copper formation, highlighting the significance of continental subduction processes in metallogenic models.

INTRODUCTION

Porphyry copper deposits (PCDs), supplying ~60% of global Cu reserves, typically occur in magmatic arcs and are genetically associated with oxidized calc-alkaline arc magmas (*1*–*3*). These magmas are oxidized because they originate from partial melting of the mantle wedge above active subduction zones, which is metasomatized by oxidized fluids and melts of the subducting slab (*4*–*10*). The elevated oxidation state in these magmas enhances Cu solubility, allowing metal transport until magma ascends to the shallow crust where copper precipitates as sulfide minerals in hydrothermal systems (*1*, *11*, *12*). Intriguingly, recent studies have shown that PCDs can also develop in postsubduction environments, such as those associated with the oxidized adakite-like, calc-alkaline porphyries in the Alpine-Himalayan orogenic belt (*13*–*16*). The genesis of these deposits remains debated because of the absence of active subduction inputs, which makes unclear the ultimate origin of the oxidized fluids forming them. Although some researchers argue that the high oxidation state of the postsubduction ore-forming porphyries can result from endogenic oxidation processes, such as garnet fractionation during synmagmatic crustal thickening (*17*, *18*), other studies emphasize the potential influence of subduction-modified lower crustal magmas and metasomatized mantle–derived ultrapotassic mafic magmas in the formation of these highly oxidized porphyries (*14*, *19*–*21*). The Gangdese porphyry copper belt, situated within the Neo-Tethys domain, lacks notable PCDs related to the subduction of the Neo-Tethys oceanic slab. Instead, it hosts several large to giant Miocene postcollisional PCDs with a total resource of >45 million tons of copper (Fig. 1) (*22*). This unique temporal and geodynamic framework makes the Gangdese belt an exceptional natural laboratory for investigating magma oxidation processes in postsubduction tectonic settings.

While direct magma redox measurements are challenging, proxies like whole-rock V/Sc (*23*) and zircon trace elements (*24*, *25*) offer robust constraints. Furthermore, mercury (Hg) isotopes are increasingly recognized as a powerful tool for tracking the recycling of volatile elements, such as those from Earth's surface marine and terrestrial systems into the mantle (*26*, *27*). Similarly, magnesium (Mg) isotopes can be used to trace recycled carbonates in the mantle, which is important for understanding subduction processes and mantle evolution (*28*–*30*). Therefore, combining Mg and Hg isotopic systems with whole-rock and zircon compositions offers a promising approach to investigating the link between mantle metasomatism and variations in magmatic oxidation states.

In this study, we analyzed whole-rock and zircon compositions in 62 igneous rocks and Mg-Hg isotopes in 52 igneous rocks from the Gangdese belt. The samples include 34 precollisional rocks, 31 syncollisional rocks, and 49 postcollisional rocks.

RESULTS

Geological background and samples

The Gangdese belt originated as part of an accretionary orogen, which formed through the subduction of the Neo-Tethyan oceanic slab, resulting in continental arc magmatism during the Mesozoic (*31*, *32*). This region evolved into a collisional orogen at ~65 to 60 million years (Ma) as a consequence of the collision between the Indian and Asian plates (*33*–*35*). The magmatic rocks found in this belt are classified into three main groups, reflecting their formation periods and associated tectonic settings (*36*, *37*): precollisional (230 to 60 Ma), syncollisional (60 to 45 Ma), and postcollisional rocks (45 to 10 Ma). Subduction-related PCDs have been discovered only at Xiongcun, whereas postcollisional PCDs occur across the eastern Gangdese belt (Fig. 1). No economic PCDs have been recognized in association with syncollisional rocks.

[1]State Key Laboratory of Deep Earth and Mineral Exploration, Institute of Geology, Chinese Academy of Geological Sciences, Beijing 100037, China. [2]State Key Laboratory of Geological Processes and Mineral Resources, China University of Geosciences, Beijing 100083, China. [3]Department of Earth Sciences, University of Geneva, Rue des Maraîchers 13, Geneva 1205, Switzerland. [4]RSC, West Perth, WA 6005, Australia. [5]Centre for Exploration Targeting and School of Earth and Oceans, The University of Western Australia, Crawley, WA 6009, Australia. [6]State Key Laboratory of Ore Deposit Geochemistry, Institute of Geochemistry, Chinese Academy of Sciences, Guiyang 550081, China.
*Corresponding author. Email: zm.yang@hotmail.com (Z.Y.); sunxiang@cugb.edu.cn (X.S.)

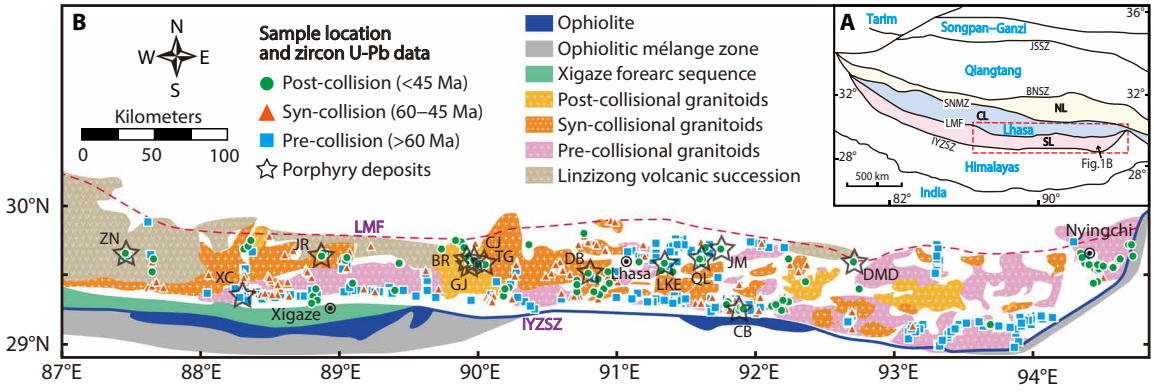

Fig. 1. Geological map of the Tibetan collisional orogen. (**A**) Simplified tectonic framework of the Tibetan Plateau. (**B**) Geological map of the eastern part of southern Lhasa Terrane showing the distribution of the Gangdese Batholith. NL, Northern Lhasa Terrane; CL, Central Lhasa Terrane; SL, Southern Lhasa Terrane; SNMZ, Shiquan River-Nam Tso mélange zone; LMF, Luobadui-Milashan Fault; IYZSZ, Indus-Yarlung Zangbo suture zone; BNSZ, Bangong-Nujiang suture zone; JSSZ, Jinshajiang suture zone; ZN, Zhunuo; XC, Xiongcun; JR, Jiru; BR, Bairong; GJ, Gangjiang; CJ, Chongjiang; TG, Tinggong; DB, Dabu; LKE, Lakang'e; QL, Qulong; JM, Jiama; CB, Chengba; DMD, Demingding.

Our dataset consists of 2050 samples, including new and published data of whole-rock and mineral geochemistry, and 283 Mg-Hg isotope data, of which 114 were acquired in the present study (tables S1 to S3). All the whole-rock V/Sc and zircon ΔFMQ [the log fO_2 (oxygen fugacity) deviation from the fayalite-magnetite-quartz (FMQ) buffer] data, where higher values of these parameters indicate a higher magmatic oxidation state (*24*), along with the whole-rock Sr/Y ratios (where higher values indicate greater magmatic water content) (*38*), are plotted as contour maps to illustrate their spatial distributions across the Gangdese belt (Fig. 2).

Whole-rock and zircon compositions

The Sr/Y values range from 0.1 to 540 (median: 33; $n = 1093$) for the precollisional rocks and from 0.5 to 121 (median: 23; $n = 301$) for the syncollisional rocks (Fig. 2). In comparison, the postcollisional rocks have elevated Sr/Y ratios of 1.7 to 217 (median: 78; $n = 443$), particularly in the ore-forming porphyries, which have Sr/Y ratios ranging from 41 to 186 (median: 94; $n = 123$).

The V/Sc ratios range from 0.43 to 35.6 (median: 9.5; $n = 868$) for the precollisional rocks, from 1.5 to 22.0 (median: 9.2; $n = 213$) for the syncollisional rocks, and from 0.7 to 25.8 (median: 11.0; $n = 311$) for the postcollisional rocks (Fig. 2). In particular, the postcollisional ore-forming porphyries have V/Sc ratios ranging from 6.3 to 22.4 (median: 11.3; $n = 76$). These values are comparable to previously reported Cu ore-forming porphyry intrusions with V/Sc > 10 (*23*) and are higher than mid-ocean ridge basalts, which have V/Sc values of 6.74 ± 1.11 (*39*).

The zircon ΔFMQ values range from −1.2 to 2.6 (median: 1.0; $n = 73$) for the precollisional rocks and from −2.5 to 2.7 (median: 0.4; $n = 45$) for the syncollisional rocks (Fig. 2). Notably, the postcollisional rocks have overall higher zircon ΔFMQ values ranging from −0.5 to 2.6 (median: 1.5; $n = 50$), and among them, the ore-forming porphyries exhibit even higher zircon ΔFMQ values of 0.8 to 2.5 (median: 1.7; $n = 15$).

Hg and Mg isotope compositions

The pre- and syncollisional granitoids exhibit Δ^{199}Hg values near zero (−0.1 to 0.14‰) (Fig. 3), similar to the estimated primitive mantle value (0 ± 0.1‰) (*40*). While overlapping with the mantle range, the postcollisional ore-forming porphyries and ultrapotassic rocks show a broader spread in Δ^{199}Hg values, particularly toward negative values, with porphyries ranging from −0.25 to 0.22‰ and ultrapotassic rocks from −0.54 to 0.25‰.

The δ^{26}Mg values range from −0.37 to −0.16‰ (mean: −0.22‰; $n = 9$) for the precollisional granitoids and from −0.23 to −0.07‰ (mean: −0.17‰; $n = 9$) for the syncollisional granitoids. Postcollisional rocks, in comparison, exhibit a wider spread in δ^{26}Mg values. The postcollisional ore-forming porphyries range from −0.39 to −0.06‰ (mean: −0.17‰; $n = 19$), whereas the ultrapotassic rocks display an even broader range from −0.51 to −0.04‰ (mean: −0.31‰; $n = 128$) (Fig. 4).

DISCUSSION

Increasing the magmatic oxidization state from subduction to collision

Our mapping of whole-rock V/Sc ratios and zircon ΔFMQ in the Gangdese belt reveals a distinct increase in magmatic oxidation state from precollision to postcollision stages (Fig. 2). The precollisional arc igneous rocks exhibit a broad range of V/Sc ratios and zircon ΔFMQ values (Fig. 2), indicating substantial variability in the oxidation state of arc magmas associated with the subduction of the Neo-Tethys oceanic slab. This variability aligns with previous studies suggesting that the oxidation state of the mantle wedge and related arc magmas in subduction zones is heterogeneous because of the input of fluids and melts derived from the subducted slab (*4*, *7*, *41*–*43*). The domains with high V/Sc ratios and zircon ΔFMQ values indicate highly oxidized arc magmas, such as the Jurassic porphyries associated with Cu-Au mineralization at Xiongcun, which is consistent with the general characteristics of arc magmas associated with PCD formation.

Zircon ΔFMQ values of the syncollisional rocks maintain broad dispersion patterns yet exhibit a downward shift in median values relative to precollisional rocks (Fig. 2). This suggests a transient decrease in magmatic fO_2. However, localized peaks in zircon ΔFMQ—such as those in southwestern Lhasa—indicate that oxidized melts were still sporadically generated, perhaps due to localized remelting of the metasomatized lower crust.

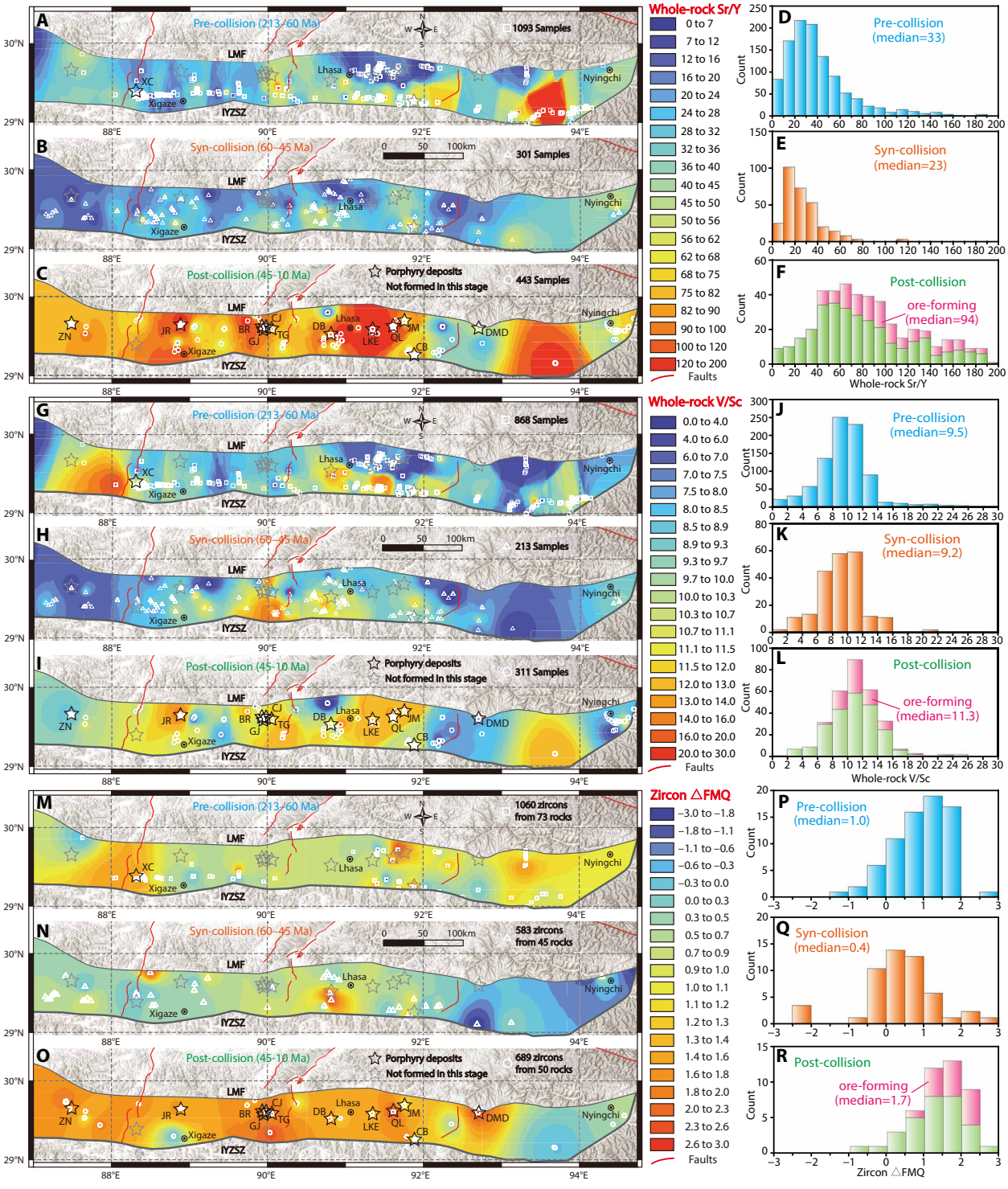

Fig. 2. Contour maps and histograms of whole-rock Sr/Y, whole-rock V/Sc, and zircon ΔFMQ from pre-, syn-, and postcollisional igneous rocks. (**A** to **C**) Contour maps of whole-rock Sr/Y. (**D** to **F**) Histograms of whole-rock Sr/Y. (**G** to **I**) Contour maps of whole-rock V/Sc. (**J** to **L**) Histograms of whole-rock V/Sc. (**M** to **O**) Contour maps of zircon ΔFMQ. (**P** to **R**) Histograms of zircon ΔFMQ. Whole-rock data are provided in table S1, and zircon data are provided in table S2. Abbreviations of deposit names are the same as in Fig. 1.

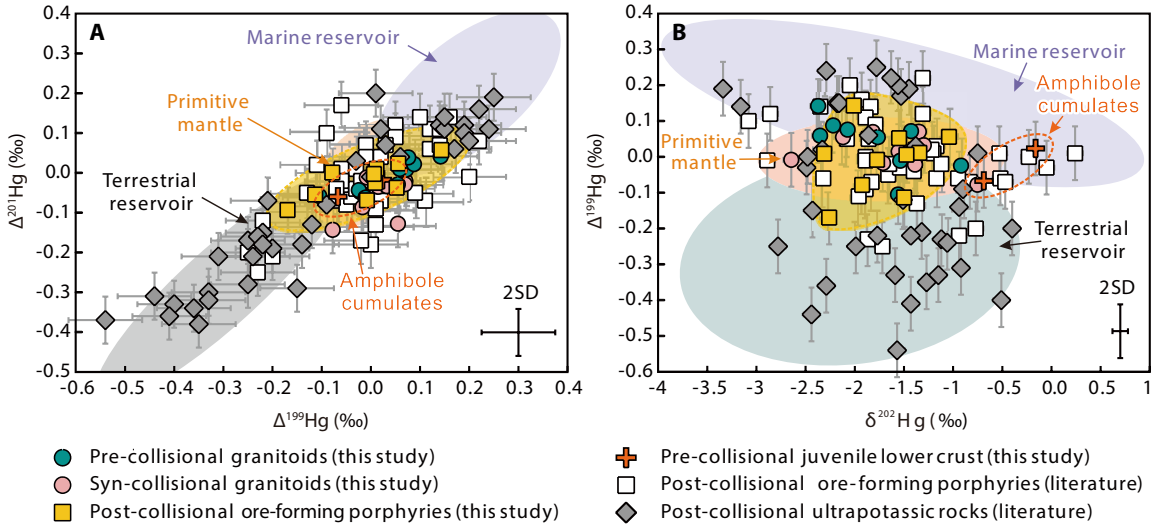

Fig. 3. Mercury isotopic compositions for the Gangdese rocks. (**A**) Δ^{201}Hg versus Δ^{199}Hg. (**B**) Δ^{199}Hg versus δ^{202}Hg. Fields for marine reservoir, terrestrial reservoir, and primitive mantle are from (*27*). Mercury isotopic data are provided in table S3.

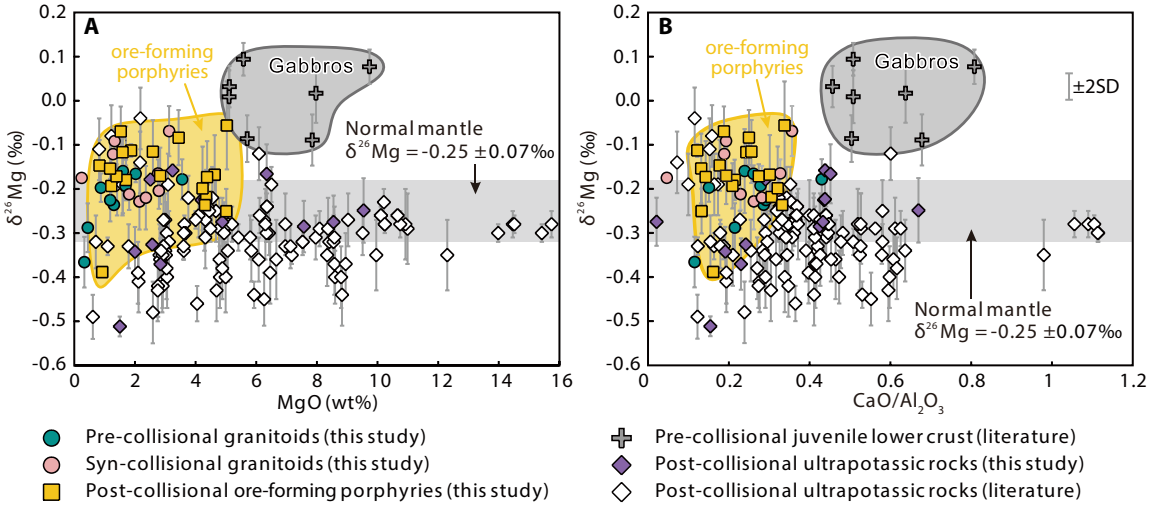

Fig. 4. Magnesium isotopic compositions for the Gangdese rocks. (**A**) δ^{26}Mg versus MgO. (**B**) δ^{26}Mg versus CaO/Al_2O_3. Error bars for δ^{26}Mg are ±2SD. The δ^{26}Mg value of normal mantle is from (*29*). Magnesium isotopic data are provided in table S3.

In contrast, postcollisional magmas display consistently elevated zircon ΔFMQ values and V/Sc values, notably higher than their pre- and syncollisional counterparts, indicating a uniformly oxidized magmatic signature. This enhanced oxidation state is most pronounced between longitudes 87°E and 92°E, which coincides spatially with Miocene porphyry Cu deposits (Fig. 2).

Recycling of carbonates from the Indian continental plate into the Tibetan lithosphere during the Indo-Asian collision

The postcollisional ore-forming porphyries and mantle-derived ultrapotassic rocks exhibit elevated Th/Yb and Th/La ratios relative to the pre- and syncollisional granitoids and mafic rocks (Fig. 5). These trace element systematics point to a dominant contribution of sediment melts to the mantle source of postcollisional magmas, as Th is simply more enriched than La and Yb in subducted sediments (*44*, *45*). Further insights into the nature of the recycled sedimentary component are provided by Lu/Hf systematics. The postcollisional rocks display notably lower Lu/Hf ratios compared to pre- and syncollisional granitoids and mafic rocks (Fig. 5D), suggesting a substantial contribution from terrigenous sediments, which typically contain abundant detrital zircon and are therefore enriched in Hf (*46*). This interpretation is further supported by zircon oxygen isotopic data from postcollisional ultrapotassic rocks, which yield δ^{18}O values ranging from ~6 to ~9‰ (fig. S1), substantially higher than mantle-derived zircon (~5.3 ± 0.3‰) (*47*). Collectively, these geochemical and isotopic observations indicate a substantial increase in the flux of terrigenous sediments into the lithospheric mantle following the India-Asia collision.

Considering that the increased involvement of terrigenous sediments in the subarc mantle began around 45 Ma, it is likely that

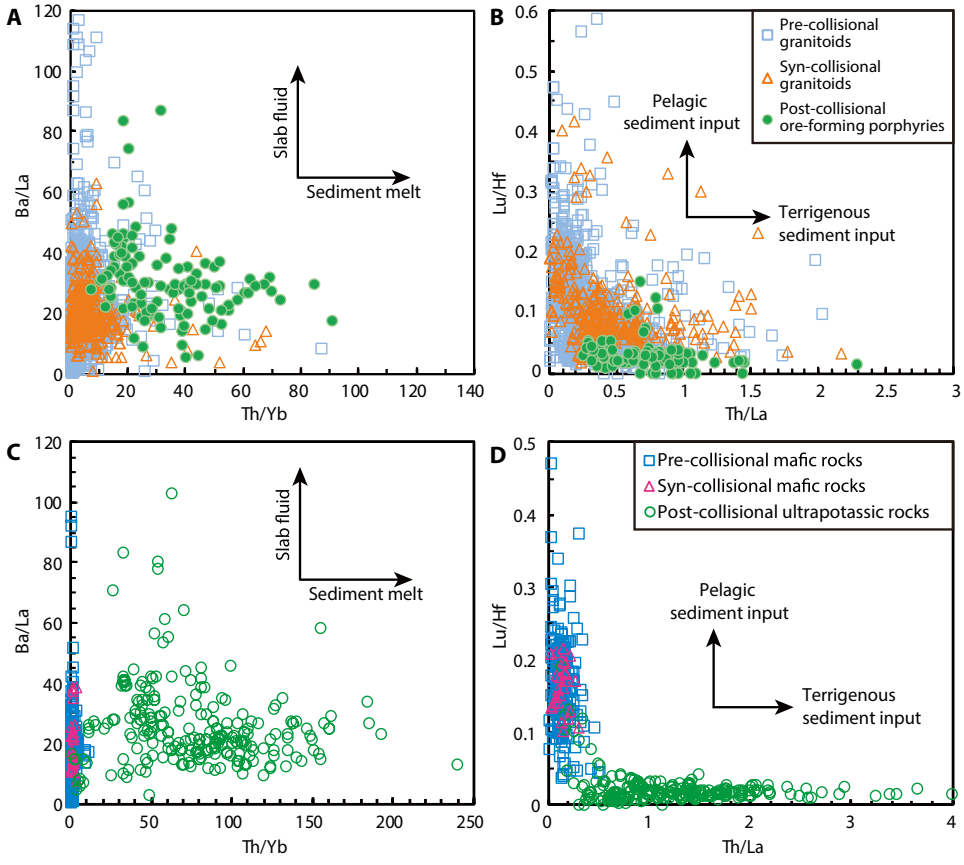

Fig. 5. Whole-rock trace element ratios for the Gangdese rocks. (**A** and **B**) Ba/La versus Th/Yb and Lu/Hf versus Th/La for the granitoids. (**C** and **D**) Ba/La versus Th/Yb and Lu/Hf versus Th/La for the mafic rocks and mantle-derived ultrapotassic rocks. The data source is the same as Fig. 2.

these sediments were sourced from the northern Indian passive margin. This inference is further supported by whole-rock Sr-Nd isotopic and zircon Hf isotopic compositions. The postcollisional ore-forming porphyries and mantle-derived mafic magmas exhibit high initial Sr isotopic ratios and lower Nd isotopic ratios compared to their pre- and syncollisional counterparts (fig. S2). In addition, our mapping of zircon Hf isotopic compositions in the Gangdese belt using literature data reveals a distinct decrease in $\varepsilon_{Hf}(t)$ values from precollision to postcollision stages (fig. S3). These observations rule out the possibility that the terrigenous sediments were derived from the weathering and erosion of the pre- and syncollisional igneous rocks in the southern Lhasa Terrane, which has been suggested to be isotopically depleted via zircon Hf isotopic mapping (*48*). The postcollisional mafic rocks have higher $^{87}Sr/^{86}Sr$ and lower $\varepsilon_{Nd}(t)$ values than pre- and syncollision rocks (fig. S2). This suggests that the isotopic characteristics of the postcollisional rocks are primarily inherited from their source rather than resulting from increased crustal assimilation. Therefore, these terrigenous sediments most likely originated from the northern Indian continent.

Hg isotopes exhibit both mass-dependent fractionation (typically reported as $\delta^{202}Hg$) and mass-independent fractionation (MIF; typically reported as $\Delta^{199}Hg$) (*26*). The MIF of Hg isotopes in igneous rocks is not influenced by magmatic, metamorphic, or hydrothermal processes but instead reflects Earth's surface reservoirs, which can be recycled into magma sources through plate tectonics (*27*, *49*, *50*). The lack of correlations between SiO_2 concentrations and $\Delta^{199}Hg$ or $\delta^{202}Hg$ values (fig. S4) indicates that Hg-isotope variations are not related to magma differentiation. All samples show a positive correlation between $\Delta^{199}Hg$ and $\Delta^{201}Hg$ with a slope of 1.00 ± 0.17 (fig. S5), which is indistinguishable, within uncertainty, from the correlation observed in aqueous Hg(II) (divalent mercury species) photoreduction (slope of 1.00 ± 0.02) (*26*). The pre- and syncollisional granitoids exhibit $\Delta^{199}Hg$ values similar to the estimated primitive mantle value (*40*), whereas the postcollisional ore-forming porphyries display more variable and, in many cases, more negative $\Delta^{199}Hg$ values (Fig. 3). The pronounced Hg-MIF signatures suggest the addition of ancient terrestrial Hg via the subduction of Indian continental sediments into the crustal sources, as terrestrial materials typically exhibit negative $\Delta^{199}Hg$ values (*27*, *51*). Similarly, the postcollisional ultrapotassic mafic rocks, which are interpreted to originate from partial melting of the metasomatized lithospheric mantle (*19*, *20*), also show pronounced Hg-MIF signals with negative $\Delta^{199}Hg$ values. This further indicates the recycling of ancient Indian terrestrial Hg into the Tibetan lithospheric mantle.

Mg isotopes further demonstrate the recycling of carbonates into the Tibetan lithospheric mantle. The high CaO/Al_2O_3 ratios of the postcollisional ultrapotassic mafic rocks indicate an essential role of carbonate melts in the petrogenesis of these rocks (Fig. 4), because carbonated melts are characterized by high CaO/Al_2O_3 (*52*). Most ultrapotassic mafic rocks in the Gangdese belt exhibit lower $\delta^{26}Mg$

values compared to those of the primitive mantle or mid-ocean ridge basalts (*29*). These δ^{26}Mg values are notably lower than those of the pre- and syncollisional granitoids (Fig. 4), ruling out the involvement of terrigenous sediments from the southern Lhasa Terrane. Given that partial melting does not substantially fractionate Mg isotopes and carbonates have inherently lighter δ^{26}Mg values (*30*, *53*), the isotopically light Mg signature observed in the ultrapotassic rocks is best interpreted as a geochemical fingerprint of recycled carbonate material. This interpretation is further supported by the lack of correlation between δ^{26}Mg and SiO_2 contents (fig. S6), which rules out differentiation processes or upper crustal assimilation as primary controls on the isotopic variability. The inferred carbonate input likely originated from the subducted northern Indian continental margin, which is known to host thick carbonate-bearing sedimentary sequences. These include platform and basinal carbonates of the Tethyan Himalayas, Ladakh Himalaya, and Eastern Pontides, which formed during the Mesozoic to Eocene and locally reach several kilometers in thickness (*54*–*56*). The substantial volume and regional extent of these sedimentary carbonates make them a plausible and volumetrically notable source of recycled material during the India-Asia continental collision.

While both the postcollisional ultrapotassic rocks and the ore-forming porphyries display Hg-Mg isotopic evidence for sediment-derived signatures, the signal from recycled carbonate is more pronounced in the ultrapotassic rocks (Figs. 3 and 4). This difference likely reflects their contrasting petrogenetic origins. Ultrapotassic rocks are typically mantle derived and form from low-degree partial melting of a metasomatized lithospheric mantle (*19*, *20*, *57*), making them more sensitive to carbonate addition. In contrast, porphyry-forming felsic magmas are primarily derived from juvenile lower crustal sources (*14*), where the isotopic signatures may be more diluted or modified by crustal processes. Despite these differences, the consistent isotopic trends between these two rock types suggest that both ultimately record the recycling of carbonates into the mantle and/or lower crust during continental subduction.

Cause of elevated magmatic fo_2 from oceanic subduction to postcollision

Intracrustal oxidation attended by Fe depletion coupled with fractionation of Fe-rich garnet is an important mechanism to increase the oxidation of calc-alkaline arc magmas (*17*, *58*). In the Gangdese arc, the presence of an amphibole-dominated arc root (*59*, *60*) and the decreasing Dy/Yb ratios observed in the postcollisional ore-forming porphyries with magmatic fractionation (fig. S7A) indicate that amphibole fractionation plays a dominant role. Furthermore, whole-rock V/Sc ratios and zircon ΔFMQ values for the postcollisional ore-forming porphyries show no clear trends with magmatic fractionation (fig. S7, B and C). The least evolved postcollisional ore-forming porphyries exhibit elevated V/Sc ratios and zircon ΔFMQ values. Therefore, we propose that magma sources might be responsible for the highly oxidized signature of these postcollisional ore-forming porphyries rather than intracrustal processes.

A fo_2 increase in the magma source can be caused by the addition of oxidized components into the mantle via oceanic slab subduction (*4*, *9*). However, the Gangdese postcollisional ore-forming porphyries were emplaced between 18 and 13 Ma (*22*), ~40 to 50 Ma after the initial collision of India with Asia (*34*). Thus, it is unlikely that the elevated oxidation state of these postcollisional ore-forming porphyries is related to the input of fluids or melts derived from the Neo-Tethys oceanic slab. A more plausible mechanism for the elevated magmatic oxidation state observed during the postcollisional stage involves the subduction of carbonate-rich lithologies and/or terrigenous sediments from the Indian continental plate into the Tibetan lithospheric mantle. This process may have triggered oxidation in the overlying lithosphere through redox reactions involving Ca-carbonates. Experimental studies at 3 GPa and 900°C demonstrate that Ca-carbonate can oxidize ferrous iron in silicates via the reaction (*61*)

$$4Fe^{2+}\ (\text{olivine}) + C^{4+}\ (\text{Ca}-\text{carbonate}) = 4Fe^{3+}\ (\text{spinel}) + C^{0}\ (\text{graphite}) \quad (1)$$

This redox mechanism is capable of increasing the ferric iron content in mantle silicates, thereby raising the whole fo_2 of the lithospheric mantle. Moreover, recent experiments conducted at high pressures (2.5 GPa) and temperatures (750° to 1050°C) have demonstrated that carbonate melts are capable of capturing sulfur in the form of sulfate from mantle peridotite and pyroxenite (*62*). Collectively, these findings suggest that sedimentary carbonates, transported by the subducted Indian continental plate into the Tibetan lithospheric mantle and/or lower crust, could have acted as oxidizing agents and enhanced the fo_2 of postcollisional magmas.

In addition, evaporite rocks, including sulfates, are found alongside carbonate rocks in the northern margin of the Indian continent (*54*). As the Indian plate subducted, these oxidized sediments underwent dehydration, releasing oxidized fluids that interacted with the overlying lithosphere, thus forming a highly oxidized mantle source region for postcollisional magmas. Therefore, the addition of evaporite sulfates into the Tibetan lithosphere during the subduction of the Indian plate can also help explain the elevated magmatic fo_2 of postcollisional ore-forming porphyries in the Gangdese belt.

Updated genetic model for postsubduction porphyry copper mineralization

PCDs in subduction zones are typically associated with the release of oxidized melts and fluids from the subducted oceanic lithosphere, which metasomatize the overlying mantle wedge, leading to the generation of highly oxidized, metal-rich arc magmas (Fig. 6A) (*4*–*10*). However, the mechanisms driving the elevated oxidation state of postcollisional PCDs remain poorly understood. The Hg and Mg isotope results of our study suggest that the oxidation of postcollisional magmas in the Gangdese belt was driven by the subduction of continental sediments, particularly carbonates and/or sulfates, from the Indian plate into the Tibetan lithosphere (Fig. 6B). The collision between the Indian and Asian plates resulted in the cessation of oceanic subduction and the initiation of continental subduction, leading to the incorporation of Indian continental sediments into the Tibetan lithosphere during the postcollisional stage. Elevated magma fo_2 leads to a shift in the dissolved sulfur species in porphyry magmas, from being predominantly in the form of sulfides to being predominantly in the form of sulfates (*63*, *64*). This sulfur oxidation raises the magmatic sulfur saturation point, allowing for higher magmatic sulfur concentrations (*65*, *66*). As a result, copper (and other chalcophile elements) remains in the magma rather than being captured by magmatic sulfides until it is later precipitated as copper-bearing minerals from fluids released by the magma to form PCDs (*1*, *11*, *67*).

Our study highlights that the postcollisional setting, where continental sediments are subducted and recycled, can also generate

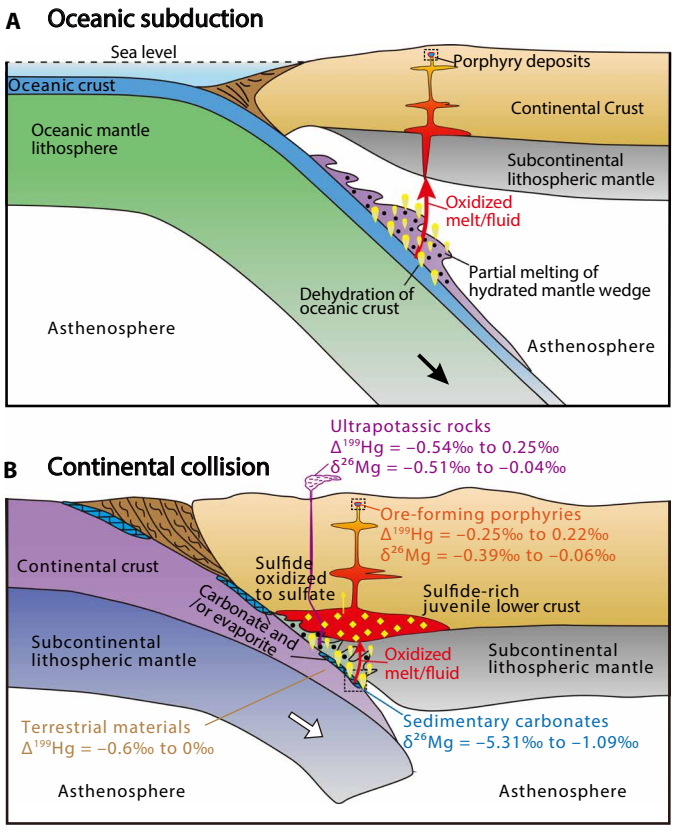

Fig. 6. Evolution of magmatic redox from oceanic subduction to continental collision. (**A**) During oceanic slab subduction, the involvement of oxidized fluids and/or melts released from the subducting slab controls the redox state of the overlying mantle wedge and the resulting arc magmas. Arc magmas associated with PCDs are highly oxidized, as their mantle sources have been metasomatized by oxidized fluids and melts. (**B**) During postcollision, the addition of oxidized sediments, such as carbonates and/or evaporite sulfates from the subducting continent, elevates the oxidation state of the lithosphere in the overlying continent and the postcollisional magmas, thereby facilitating the formation of PCDs. As a result, the distribution of oxidized sediments in passive continental margins plays a key role in the distribution of highly oxidized rocks and PCDs. The Δ^{199}Hg values of terrestrial materials are from (*27*). The δ^{26}Mg values of sedimentary carbonates are from (*30*).

highly oxidized magmas conducive to porphyry copper mineralization. This challenges the conventional view that oceanic subduction is the dominant driver of porphyry copper formation and underscores the importance of considering continental subduction processes in metallogenic models. This insight not only expands the geodynamic framework for porphyry copper formation but also opens additional directions for exploration in other collisional orogens, such as the Zagros belt and the Lesser Caucasus, where similar tectonomagmatic conditions and porphyry copper mineralization have been reported (*68*, *69*).

MATERIALS AND METHODS

Materials

This study focuses on magmatic rocks from the eastern Gangdese belt (87°E to 95°E) (Fig. 1). To obtain better spatial coverage along the belt, we collected some samples from those areas with low sample density. Our combined lithogeochemical and geochronological data, including both newly acquired and previously published data, comprise a dataset of 2050 igneous rocks ranging in age from the Late Triassic to Miocene. These samples are subdivided into precollisional (210 to 60 Ma), syncollisional (60 to 45 Ma), and postcollisional (45 to 10 Ma) suites based on the timing of initial collision between India and Asia at ~60 Ma and the loss of the pull force from the subducting oceanic slab because of its breakoff at ~45 Ma (*37*).

Analytical methods

Whole-rock major and trace element analyses

The whole-rock major element and loss-on-ignition analyses were conducted at the National Research Center for Geoanalysis, Chinese Academy of Geological Sciences (Beijing). Whole-rock major element and loss-on-ignition analyses followed the GB/T 14506.28-2010 and GB/T 14506.34-2019 standards, respectively. Major elements were analyzed by wavelength-dispersive x-ray fluorescence spectrometry (Malvern Panalytical, AXIOS-PW4400). The 2SD uncertainties for all major elements are <2% relative. The samples (25 mg) were digested in a sealed vessel with 0.5 ml of nitric acid and 1.5 ml of hydrofluoric acid and then heated for 48 hours to ensure complete dissolution. Trace elements, including the rare earth elements, were analyzed by inductively coupled plasma mass spectrometry (ICP-MS) using an Agilent 7500a system. Three international standards (GSR-1, GSR-3, and GSR-5) were used to assess the analytical reproducibility. The 2SD uncertainties are <10% for elements with abundances <10 ppm (parts per million) and <5% relative for those >10 ppm. A total of 62 whole-rock major and trace elements were analyzed, and the data are listed in table S1.

Zircon U-Pb dating and trace element analyses

Zircon grains were separated from igneous rocks and mounted in epoxy resin for age and trace element determinations. Zircon U-Pb dating and trace element analyses were conducted simultaneously by laser ablation ICP-MS in the Mineral and Fluid Inclusion Microanalysis Laboratory, Institute of Geology, Chinese Academy of Geological Sciences, Beijing, China. The NWR 193^{UC} laser ablation system (Elemental Scientific Lasers, US) was equipped with a Coherent Excistar 200 excimer laser and a two-volume ablation cell. The laser ablation system was coupled to an Agilent 7900 ICP-MS instrument (Agilent, US). Zircons were mounted in epoxy resin discs, polished to expose grain interiors, cleaned ultrasonically in ultrapure water, and then cleaned again before analysis using analytical-grade methanol. Preablation was conducted before each spot analysis using five laser shots (~0.3 μm in depth) to remove potential surface contamination. The analyses used a 30-μm laser beam diameter with a laser frequency of 8 Hz and a fluence of 2 J/cm^2. The Iolite software package was used for data reduction (*70*). Zircons 91500 and SA01 were the primary and secondary reference materials, respectively. The exponential function was used to correct for down-hole fractionation (*71*). NIST 610 and ^{91}Zr were used to calibrate the trace element concentrations as an external reference material and internal standard, respectively. A total of 1477 zircon grains from 82 magmatic rocks was analyzed. Zircon age and trace element data are listed in table S2.

Hg isotope analyses

Hg concentrations and Hg isotope ratios were measured at the State Key Laboratory of Ore Deposit Geochemistry, Institute of Geochemistry, Chinese Academy of Sciences in Guiyang. Hg in rock powder was extracted using a dual-stage tube furnace using a catalyst-containing

furnace quartz tube, with the detailed testing procedure described in the previous literature (*72*). After a combustion-trapping procedure, the trapping solution was transferred into a 40-ml lucifugal borosilicate glass bottle (precleaned at 480°C in a muffle furnace for 1.5 hours) at 4°C before trace element concentration, Hg concentration, and Hg isotopic composition analyses. Hg recoveries of 90 to 110% and uncertainties of <10% (2SD) were obtained. The total Hg concentrations of samples were directly measured using a Milestone DMA-80 Hg analyzer. The sample solutions were diluted to 1 ng/ml Hg in 10 to 20% (v/v) reverse aqua regia (HNO_3/HCl = 2/1, v/v) using 18.2 megohms·cm water. Analysis of the Hg isotopic composition was done using Neptune Plus multicollector ICP-MS. Instrumental mass bias was corrected using a NIST SRM 997 Tl standard solution [25 ng/ml Tl in 3% (v/v) HNO_3] introduced by an Aridus II desolvating nebulizer. The Hg isotopic composition was reported following the convention recommended by Bergquist and Blum (*26*). The overall average and uncertainty of NIST-3177 (δ^{202}Hg, −0.53 ± 0.08‰; Δ^{199}Hg, −0.01 ± 0.07‰; Δ^{200}Hg, 0.02 ± 0.09‰; and Δ^{201}Hg, −0.03 ± 0.06‰; 2SD, n = 24), GSR-2 (δ^{202}Hg, −1.48 ± 0.13‰; Δ^{199}Hg, −0.00 ± 0.10‰; Δ^{200}Hg, 0.05 ± 0.06‰; and Δ^{201}Hg, −0.08 ± 0.05‰; 2SD, n = 3), and GSS-4 (δ^{202}Hg, −1.67 ± 0.18‰; Δ^{199}Hg, −0.38 ± 0.11‰; Δ^{200}Hg, −0.09 ± 0.20‰; and Δ^{201}Hg, −0.42 ± 0.16‰; 2SD, n = 3) agree well with previous results (*27*, *40*, *73*, *74*), and all results are listed in table S3.

Mg isotope analyses

Mg isotope ratio analyses were carried out at the MNR Key Laboratory of Isotope Geology, Institute of Geology, Chinese Academy of Geological Sciences. Approximately 10 to 30 mg of sample powders was weighed into precleaned Savillex PFA beakers and digested using a 3:1 mixture of HF and HNO_3 on a hot plate at 120°C for >48 hours. After digestion, samples were further treated with aqua regia until they were fully dissolved. Mg was purified using a one-stage column procedure with Bio-Rad AG50W-X12 cation resin (200 to 400 mesh). Around 10 μg of Mg in 0.7 M HNO_3 was loaded onto the column, which contained 1.78 ml of precleaned resin. Matrix elements (Al, Ti, Fe, Li, Na, and K) were removed using 50 ml of 0.7 M HNO_3 and 0.2 M HF, and Mg was eluted with 8 ml of 2 M HNO_3. After one purification step, matrix elements were effectively removed. At least one basaltic standard (BHVO-2 and GSR-3) and a duplicate were processed with each batch.

Mg isotope ratios were measured on a Nu Plasma II multicollector ICP-MS in low-resolution mode, with standard-sample bracketing used to correct for mass fractionation. Samples with Mg (~1 μg/ml) were introduced into the mass spectrometer in 0.3 M HNO_3 using a microconcentric quartz nebulizer at a flow rate of ~30 μl min^{-1}. Ion beams for ^{24}Mg, ^{25}Mg, and ^{26}Mg were measured on the L5, H1, and H6 Faraday cups. Each measurement included 100 cycles of 3-s integration time. A blank (0.3 M HNO_3) was measured at the beginning of each session for on-peak-zero correction. The difference in Mg concentration between samples and standards was less than 10%. Mg isotope compositions were reported relative to the DSM-3 standard (a solution in 3% HNO_3 made from pure Mg metal) (*75*) using the equation (i = 25 or 26)

$$\delta^{i}\mathrm{Mg}(‰) = \left[\left({}^{i}\mathrm{Mg}/{}^{24}\mathrm{Mg}\right)_{\mathrm{sample}}/\left({}^{i}\mathrm{Mg}/{}^{24}\mathrm{Mg}\right)_{\mathrm{DSME}} - 1\right] \times 1000 \quad (2)$$

where i is 25 or 26, $({}^{i}\mathrm{Mg}/{}^{24}\mathrm{Mg})_{\mathrm{DSM3}}$ is the ^{i}Mg/^{24}Mg ratio of DSM-3, and $({}^{i}\mathrm{Mg}/{}^{24}\mathrm{Mg})_{\mathrm{sample}}$ is the ^{i}Mg/^{24}Mg ratio of studied samples. The overall average and uncertainty of BHVO-2 (δ^{25}Mg, −0.1 ± 0.03‰; δ^{26}Mg, −0.22 ± 0.07‰; 2SD, n = 3), GSP-2 (δ^{25}Mg, 0.04 ± 0.02‰; δ^{26}Mg, 0.07 ± 0.04‰; 2SD, n = 4), GSR-3 (δ^{25}Mg, −0.22 ± 0.02‰; δ^{26}Mg, −0.45 ± 0.05‰; 2SD, n = 4), and seawater (δ^{25}Mg, −0.43 ± 0.04‰; δ^{26}Mg, −0.84 ± 0.04‰; 2SD, n = 4) agree well with previous results (*76*–*78*), and all results are listed in table S3.

Mapping strategy

Whole-rock and zircon geochemical contour maps were undertaken in ArcGIS Pro using the inverse distance weighted interpolation, which represents the best combination of mapping methods (*79*, *80*). All data were grouped by the geometrical interval method with some manual adjustment, ensuring that each group had approximately the same number of values and more geological significance. The geographic coordinate system is the World Geodetic System 1984. All zircon data shown in contour maps represent the mean values of each rock.

Supplementary Materials

The PDF file includes:

Figs. S1 to S7

Legends for tables S1 to S4

Other Supplementary Material for this manuscript includes the following:

Tables S1 to S4

REFERENCES AND NOTES

1. J. P. Richards, Tectono-magmatic precursors for porphyry Cu-(Mo-Au) deposit formation. *Econ. Geol.* **98**, 1515–1533 (2003).
2. R. H. Sillitoe, Porphyry copper systems. *Econ. Geol.* **105**, 3–41 (2010).
3. L. Evenstar, S. Dahlström, A. Hartley, T. C. McCuaig, A. Mather, J. Shaw, Global constraints on exhumation rates during porphyry copper formation and supergene enrichment: Applications to exploration as illustrated from the Central Andes. *Miner. Deposita* **60**, 23–45 (2025).
4. K. A. Kelley, E. Cottrell, Water and the oxidation state of subduction zone magmas. *Science* **325**, 605–607 (2009).
5. C.-T. A. Lee, P. Luffi, V. Le Roux, R. Dasgupta, F. Albaréde, W. P. Leeman, The redox state of arc mantle using Zn/Fe systematics. *Nature* **468**, 681–685 (2010).
6. K. A. Evans, M. Elburg, V. Kamenetsky, Oxidation state of subarc mantle. *Geology* **40**, 783–786 (2012).
7. W. Sun, M. Ling, X. Yang, W. Fan, X. Ding, H. Liang, Ridge subduction and porphyry copper-gold mineralization: An overview. *Sci. China Earth Sci.* **53**, 475–484 (2010).
8. P. Tollan, J. Hermann, Arc magmas oxidized by water dissociation and hydrogen incorporation in orthopyroxene. *Nat. Geosci.* **12**, 667–671 (2019).
9. J. Ague, S. Tassara, M. Holycross, J. Li, E. Cottrell, E. Schwarzenbach, C. Fassoulas, T. John, Slab-derived devolatilization fluids oxidized by subducted metasedimentary rocks. *Nat. Geosci.* **15**, 320–326 (2022).
10. W. Sun, H. Liang, M. Ling, M. Zhan, X. Ding, H. Zhang, X. Yang, Y. Li, T. R. Ireland, Q. Wei, W. Fan, The link between reduced porphyry copper deposits and oxidized magmas. *Geochim. Cosmochim. Acta* **103**, 263–275 (2013).
11. D. R. Cooke, P. Hollings, J. L. Walshe, Giant porphyry deposits: Characteristics, distribution, and tectonic controls. *Econ. Geol.* **100**, 801–818 (2005).
12. M. Chiaradia, Copper enrichment in arc magmas controlled by overriding plate thickness. *Nat. Geosci.* **7**, 43–46 (2014).
13. Z.-Q. Hou, Y.-F. Gao, X.-M. Qu, Z.-Y. Rui, X.-X. Mo, Origin of adakitic intrusives generated during mid-Miocene east–west extension in southern Tibet. *Earth Planet. Sci. Lett.* **220**, 139–155 (2004).
14. Z. Hou, Z. Yang, Y. Lu, A. Kemp, Y. Zheng, Q. Li, J. Tang, L. Duan, A genetic linkage between subduction- and collision-related porphyry Cu deposits in continental collision zones. *Geology* **43**, 247–250 (2015).
15. J. P. Richards, Postsubduction porphyry Cu-Au and epithermal Au deposits: Products of remelting of subduction-modified lithosphere. *Geology* **37**, 247–250 (2009).
16. Z. Yang, K. Cao, Post-collisional porphyry copper deposits in Tibet: An overview. *Earth Sci. Rev.* **258**, 104954 (2024).
17. M. Tang, M. Erdman, G. Eldridge, C.-T. A. Lee, The redox "filter" beneath magmatic orogens and the formation of continental crust. *Sci. Adv.* **4**, eaar4444 (2018).

18. M. Tang, C.-T. A. Lee, W.-Q. Ji, R. Wang, G. Costin, Crustal thickening and endogenic oxidation of magmatic sulfur. *Sci. Adv.* **6**, eaba6342 (2020).
19. Z.-M. Yang, Y.-J. Lu, Z.-Q. Hou, Z.-S. Chang, High-Mg diorite from Qulong in southern Tibet: Implications for the genesis of adakite-like intrusions and associated porphyry Cu deposits in collisional orogens. *J. Petrol.* **56**, 227–254 (2015).
20. X. Sun, Y.-J. Lu, T. C. McCuaig, Y.-Y. Zheng, H.-F. Chang, F. Guo, L.-J. Xu, Miocene ultrapotassic, high-Mg dioritic, and adakite-like rocks from Zhunuo in southern Tibet: Implications for mantle metasomatism and porphyry copper mineralization in collisional orogens. *J. Petrol.* **59**, 341–386 (2018).
21. X. Sun, Y. Lu, Q. Li, R. Li, A downgoing Indian lithosphere control on along-strike variability of porphyry mineralization in the Gangdese belt of southern Tibet. *Econ. Geol.* **116**, 29–46 (2021).
22. Z.-M. Yang, R. Goldfarb, Z.-S. Chang, Generation of postcollisional porphyry copper deposits in southern Tibet triggered by subduction of the Indian continental plate. *Soc. Econ. Geol. Spec. Publ.* **19**, 279–300 (2016).
23. R. R. Loucks, Distinctive composition of copper-ore-forming arcmagmas. *Aust. J. Earth Sci.* **61**, 5–16 (2014).
24. R. R. Loucks, M. L. Fiorentini, G. J. Henríquez, New magmatic oxybarometer using trace elements in zircon. *J. Petrol.* **61**, egaa034 (2020).
25. D. J. Smythe, J. M. Brenan, Magmatic oxygen fugacity estimated using zircon-melt partitioning of cerium. *Earth Planet. Sci. Lett.* **453**, 260–266 (2016).
26. B. A. Bergquist, J. D. Blum, Mass-dependent and -independent fractionation of Hg isotopes by photoreduction in aquatic systems. *Science* **318**, 417–420 (2007).
27. R. Yin, D. Chen, X. Pan, C. Deng, L. Chen, X. Song, S. Yu, C. Zhu, X. Wei, Y. Xu, X. Feng, J. D. Blum, B. Lehmann, Mantle Hg isotopic heterogeneity and evidence of oceanic Hg recycling into the mantle. *Nat. Commun.* **13**, 948 (2022).
28. J. A. Higgins, D. P. Schrag, Constraining magnesium cycling in marine sediments using magnesium isotopes. *Geochim. Cosmochim. Acta* **74**, 5039–5053 (2010).
29. F.-Z. Teng, W.-Y. Li, S. Ke, B. Marty, N. Dauphas, S. Huang, F.-Y. Wu, A. Pourmand, Magnesium isotopic composition of the Earth and chondrites. *Geochim. Cosmochim. Acta* **74**, 4150–4166 (2010).
30. S.-G. Li, W. Yang, S. Ke, X. Meng, H. Tian, L. Xu, Y. He, J. Huang, X.-C. Wang, Q. Xia, W. Sun, X. Yang, Z.-Y. Ren, H. Wei, Y. Liu, F. Meng, J. Yan, Deep carbon cycles constrained by a large-scale mantle Mg isotope anomaly in eastern China. *Natl. Sci. Rev.* **4**, 111–120 (2017).
31. A. Yin, T. M. Harrison, Geologic evolution of the Himalayan-Tibetan orogen. *Annu. Rev. Earth Planet. Sci.* **28**, 211–280 (2000).
32. W.-Q. Ji, F.-Y. Wu, S.-L. Chung, J.-X. Li, C.-Z. Liu, Zircon U–Pb geochronology and Hf isotopic constraints on petrogenesis of the Gangdese batholith, southern Tibet. *Chem. Geol.* **262**, 229–245 (2009).
33. L. Ding, P. Kapp, X. Wan, Paleocene–Eocene record of ophiolite obduction and initial India-Asia collision, south central Tibet. *Tectonics* **24**, TC3001 (2005).
34. L. Ding, P. Kapp, F. Cai, C. N. Garzione, Z. Xiong, H. Wang, C. Wang, Timing and mechanisms of Tibetan Plateau uplift. *Nat. Rev. Earth Environ.* **3**, 652–667 (2022).
35. P. Kapp, P. G. DeCelles, Mesozoic–Cenozoic geological evolution of the Himalayan-Tibetan orogen and working tectonic hypotheses. *Am. J. Sci.* **319**, 159–254 (2019).
36. X. Hu, E. Garzanti, J. Wang, W. Huang, W. An, A. Webb, The timing of India-Asia collision onset–Facts, theories, controversies. *Earth Sci. Rev.* **160**, 264–299 (2016).
37. D.-C. Zhu, Q. Wang, R. Weinberg, P. Cawood, S.-L. Chung, Y.-F. Zheng, Z.-D. Zhao, Z.-Q. Hou, X.-X. Mo, Interplay between oceanic subduction and continental collision in building continental crust. *Nat. Commun.* **13**, 7141 (2022).
38. J. P. Richards, High Sr/Y arc magmas and porphyry Cu ± Mo ± Au deposits: Just add water. *Econ. Geol.* **106**, 1075–1081 (2011).
39. Z.-X. Li, C.-T. Lee, The constancy of upper mantle fO_2 through time inferred from V/Sc ratios in basalts. *Earth Planet. Sci. Lett.* **228**, 483–493 (2004).
40. F. Moynier, M. G. Jackson, K. Zhang, H. Cai, S. A. Halldórsson, R. Pik, J. M. D. Day, J. Chen, The mercury isotopic composition of Earth's mantle and the use of mass independently fractionated Hg to test for recycled crust. *Geophys. Res. Lett.* **48**, e2021GL094301 (2021).
41. A. Bénard, K. Klimm, A. B. Woodland, R. J. Arculus, M. Wilke, R. E. Botcharnikov, N. Shimizu, O. Nebel, C. Rivard, D. A. Ionov, Oxidising agents in sub-arc mantle melts link slab devolatilisation and arc magmas. *Nat. Commun.* **9**, 3500 (2018).
42. B. Debret, M.-A. Millet, M.-L. Pons, P. Bouilhol, E. Inglis, H. Williams, Isotopic evidence for iron mobility during subduction. *Geology* **44**, 215–218 (2016).
43. W.-K. Li, Z.-M. Yang, M. Chiaradia, Y. Lai, C. Yu, J. Zhang, Redox state of southern Tibetan upper mantle and ultrapotassic magmas. *Geology* **48**, 733–736 (2020).
44. T. Kogiso, Y. Tatsumi, S. Nakano, Trace element transport during dehydration processes in the subducted oceanic crust: 1. Experiments and implications for the origin of ocean island basalts. *Earth Planet. Sci. Lett.* **148**, 193–205 (1997).
45. L. Zhao, F. Guo, W. Fan, M. Huang, Roles of subducted pelagic and terrigenous sediments in Early Jurassic mafic magmatism in NE China: Constraints on the architecture of Paleo-Pacific subduction zone. *J. Geophys. Res. Solid Earth* **124**, 2525–2550 (2019).
46. P. J. Patchett, W. M. White, H. Feldmann, S. Kielinczuk, A. W. Hofmann, Hafnium/rare earth element fractionation in the sedimentary system and crustal recycling into the Earth's mantle. *Earth Planet. Sci. Lett.* **69**, 365–378 (1984).
47. J. W. Valley, P. D. Kinny, D. J. Schulze, M. J. Spicuzza, Zircon megacrysts from kimberlite: Oxygen isotope variability among mantle melts. *Contrib. Mineral. Petrol.* **133**, 1–11 (1998).
48. Z. Hou, L. Duan, Y. Lu, Y. Zheng, D. Zhu, Z. Yang, Z. Yang, B. Wang, Y. Pei, Z. Zhao, T. C. McCuaig, Lithospheric architecture of the Lhasa terrane and its control on ore deposits in the Himalayan-Ttibetan orogen. *Econ. Geol.* **110**, 1541–1575 (2015).
49. Q. Wang, X. Liu, R. Yin, W. Weng, H. Zhao, L. Yang, D. Zhai, D. Li, Y. Ma, D. I. Groves, J. Deng, Metasomatized mantle sources for orogenic gold deposits hosted in high-grade metamorphic rocks: Evidence from Hg isotopes. *Geology* **52**, 115–119 (2024).
50. J.-Y. Zhang, K.-F. Qiu, R. Yin, Z.-Y. Long, Y.-C. Feng, H.-C. Yu, Z.-Y. Gao, J. Deng, Lithospheric mantle as a metal storage reservoir for orogenic gold deposits in active continental margins: Evidence from Hg isotopes. *Geology* **52**, 423–428 (2024).
51. J. D. Blum, L. S. Sherman, M. W. Johnson, Mercury isotopes in earth and environmental sciences. *Annu. Rev. Earth Planet. Sci.* **42**, 249–269 (2014).
52. M. J. Walter, G. P. Bulanova, L. S. Armstrong, S. Keshav, J. D. Blundy, G. Gudfinnsson, O. T. Lord, A. R. Lennie, S. M. Clark, C. B. Smith, L. Gobbo, Primary carbonatite melt from deeply subducted oceanic crust. *Nature* **454**, 622–625 (2008).
53. F.-Z. Teng, Y. Hu, C. Chauvel, Magnesium isotope geochemistry in arc volcanism. *Proc. Natl. Acad. Sci. U.S.A.* **113**, 7082–7087 (2016).
54. C. Scheibner, R. P. Speijer, Late Paleocene–early Eocene Tethyan carbonate platform evolution—A response to long- and short-term paleoclimatic change. *Earth Sci. Rev.* **90**, 71–102 (2008).
55. X. Hu, L. Jansa, C. Wang, M. Sarti, K. Bak, M. Wagreich, J. Michalik, J. Soták, Upper Cretaceous oceanic red beds (CORBs) in the Tethys: Occurrences, lithofacies, age, and environments. *Cretac. Res.* **26**, 3–20 (2005).
56. H. Willems, Z. Zhou, B. Zhang, K.-U. Gräfe, Stratigraphy of the upper cretaceous and lower tertiary strata in the tethyan himalayas of Tibet (Tingri area, China). *Geol. Rundsch.* **85**, 723–754 (1996).
57. S. Turner, N. Arnaud, J. Liu, N. Rogers, C. Hawkesworth, N. Harris, S. Kelley, P. Van Calsteren, W. Deng, Post-collision, shoshonitic volcanism on the Tibetan Plateau: Implications for convective thinning of the lithosphere and the source of ocean island basalts. *J. Petrol.* **37**, 45–71 (1996).
58. M. Tang, C.-T. A. Lee, G. Costin, H. E. Höfer, Recycling reduced iron at the base of magmatic orogens. *Earth Planet. Sci. Lett.* **528**, 115827 (2019).
59. Z. Zhang, X. Dong, H. Xiang, Z. He, J. G. Liou, Metagabbros of the Gangdese arc root, south Tibet: Implications for the growth of continental crust. *Geochim. Cosmochim. Acta* **143**, 268–284 (2014).
60. W. Xu, D.-C. Zhu, Q. Wang, R. F. Weinberg, R. Wang, S.-M. Li, L.-L. Zhang, Z.-D. Zhao, Constructing the early Mesozoic Gangdese crust in southern Tibet by hornblende-dominated magmatic differentiation. *J. Petrol.* **60**, 515–552 (2019).
61. R. Tao, Y. Fei, Recycled calcium carbonate is an efficient oxidation agent under deep upper mantle conditions. *Commun. Earth Environ.* **2**, 45 (2021).
62. I. S. Ezad, M. Saunders, S. S. Shcheka, M. L. Fiorentini, L. R. Gorojovsky, M. W. Förster, S. F. Foley, Incipient carbonate melting drives metal and sulfur mobilization in the mantle. *Sci. Adv.* **10**, eadk5979 (2024).
63. R. E. Botcharnikov, R. L. Linnen, M. Wilke, F. Holtz, P. J. Jugo, J. Berndt, High gold concentrations in sulphide-bearing magma under oxidizing conditions. *Nat. Geosci.* **4**, 112–115 (2011).
64. Z. Zajacz, P. A. Candela, P. M. Piccoli, C. Sanchez-Valle, The partitioning of sulfur and chlorine between andesite melts and magmatic volatiles and the exchange coefficients of major cations. *Geochim. Cosmochim. Acta* **89**, 81–101 (2012).
65. J. E. Mungall, J. M. Brenan, B. Godel, S. J. Barnes, F. Gaillard, Transport of metals and sulphur in magmas by flotation of sulphide melt on vapour bubbles. *Nat. Geosci.* **8**, 216–219 (2015).
66. P. J. Jugo, Sulfur content at sulfide saturation in oxidized magmas. *Geology* **37**, 415–418 (2009).
67. A. Audétat, T. Pettke, C. A. Heinrich, R. J. Bodnar, The composition of magmatic-hydrothermal fluids in barren and mineralized intrusions. *Econ. Geol.* **103**, 877–908 (2008).
68. M. Aghazadeh, Z. Hou, Z. Badrzadeh, L. Zhou, Temporal–spatial distribution and tectonic setting of porphyry copper deposits in Iran: Constraints from zircon U–Pb and molybdenite Re–Os geochronology. *Ore Geol. Rev.* **70**, 385–406 (2015).
69. R. Moritz, R. Melkonyan, D. Selby, N. Popkhadze, V. Gugushvili, R. Tayan, V. Ramazanov, Metallogeny of the lesser Caucasus: From arc construction to postcollision evolution. *Soc. Econ. Geol. Spec. Publ.* **19**, 157–192 (2016).
70. C. Paton, J. Hellstrom, B. Paul, J. Woodhead, J. Hergt, Iolite: Freeware for the visualisation and processing of mass spectrometric data. *J. Anal. At. Spectrom* **26**, 2508–2518 (2011).
71. C. Paton, J. D. Woodhead, J. C. Hellstrom, J. M. Hergt, R. Maas, Improved laser ablation U-Pb zircon geochronology through robust downhole fractionation correction. *Geochem. Geophys. Geosyst.* **11**, Q0AA06 (2010).

72. L. Gao, D. Sun, X. Wang, D. Chen, Z.-D. Tian, A. Luo, R. Yin, A catalyst tube-equipped dual-stage tube furnace system for accurate Hg isotopic determination of ore samples using Neptune plus multicollector inductively coupled plasma mass spectrometry. *Anal. Chem.* **96**, 17560–17566 (2024).
73. B. Xu, R.-S. Yin, M. Chiaradia, Z. Miao, W. L. Griffin, Z.-Q. Hou, Z.-M. Yang, S. Y. O'Reilly, Mercury isotope evidence for the importance of recycled fluids in collisional ore systems. *Sci. Adv.* **10**, eadp7383 (2024).
74. H. Geng, R. Yin, X.-D. Li, An optimized protocol of high precision measurement of Hg isotopic compositions in samples with low concentrations of Hg using MC-ICP-MS. *J. Anal. At. Spectrom* **33**, 1932–1940 (2018).
75. A. Galy, O. Yoffe, P. Janney, R. Williams, C. Cloquet, O. Alard, L. Halicz, M. Wadhwa, I. Hutcheon, E. Ramon, J. Carignan, Magnesium isotope heterogeneity of the isotopic standard SRM980 and new reference materials for magnesium-isotope-ratio measurements. *J. Anal. At. Spectrom* **18**, 1352–1356 (2003).
76. F.-Z. Teng, Q.-Z. Yin, C. V. Ullmann, R. Chakrabarti, P. A. E. Pogge von Strandmann, W. Yang, W.-Y. Li, S. Ke, F. Sedaghatpour, J. Wimpenny, A. Meixner, R. L. Romer, U. Wiechert, S. B. Jacobsen, Interlaboratory comparison of magnesium isotopic compositions of 12 felsic to ultramafic igneous rock standards analyzed by MC-ICPMS. *Geochem. Geophys. Geosystems* **16**, 3197–3209 (2015).
77. M.-X. Ling, F. Sedaghatpour, P. Hays, J. Strauss, W. Sun, Homogeneous magnesium isotopic composition of seawater: An excellent geostandard for Mg isotope analysis. *Rapid Commun. Mass Spectrom.* **25**, 2828–2836 (2011).
78. T. Gao, S. Ke, R. Li, X. Meng, Y. He, C. Liu, Y. Wang, Z. Li, J.-M. Zhu, High-precision magnesium isotope analysis of geological and environmental reference materials by multiple-collector inductively coupled plasma mass spectrometry. *Rapid Commun. Mass Spectrom.* **33**, 767–777 (2019).
79. D. R. Mole, B. M. Frieman, P. C. Thurston, J. H. Marsh, T. R. C. Jørgensen, R. A. Stern, L. A. J. Martin, Y. J. Lu, H. L. Gibson, Crustal architecture of the south-east Superior Craton and controls on mineral systems. *Ore Geol. Rev.* **148**, 105017 (2022).
80. Z.-Y. Zhang, Z.-Q. Hou, Q.-T. Lü, X.-W. Zhang, X.-F. Pan, X.-K. Fan, Y.-Q. Zhang, C.-G. Wang, Y.-J. Lü, Crustal architectural controls on critical metal ore systems in South China based on Hf isotopic mapping. *Geology* **51**, 738–742 (2023).

Acknowledgments: We thank the reviewers for insightful reviews that helped improve the paper. **Funding:** This research was funded by the National Natural Science Foundation of China (92155305), the National Key Research and Development Program of China (2022YFC2903304), and the Scientific Research Fund Project of BGRIMM Technology Group (no. JTKY202427822). **Author contributions:** Conceptualization: Z.Y. and M.C. Methodology: Z.Y., X.S., and R.Y. Resource: Z.Y., Z.H., and X.S. Funding acquisition: Z.Y. and X.S. Investigation: Z.Y., X.S., Y.L., H.L., and Y.Z. Data curation: Z.Y., X.S., and Y.Z. Formal analysis: Z.Y., X.S., Y.L., R.Y., and Y.Z. Visualization: Z.Y., X.S., H.L., and Y.Z. Supervision: Z.Y. and X.S. Project administration: Z.Y. and X.S. Validation: Z.Y. and X.S. Writing—original draft: Z.Y., X.S., and Y.L. Writing—review and editing: Z.Y., X.S., M.C., Y.L., Z.H., H.L., and Y.Z. **Competing interests:** The authors declare that they have no competing interests. **Data and materials availability:** All data needed to evaluate the conclusions in the paper are present in the paper and/or the Supplementary Materials.

Submitted 14 March 2025
Accepted 28 May 2025
Published 2 July 2025
10.1126/sciadv.adx4474